

# Exploring the duality of powder adhesion and underlying surface roughness in laser powder bed fusion processed Ti-6Al-4V

Carter, Luke; Villapun, Victor; Grover, Liam; Cox, Sophie

DOI:

[10.1016/j.jmapro.2022.06.057](https://doi.org/10.1016/j.jmapro.2022.06.057)

License:

Creative Commons: Attribution (CC BY)

*Document Version*

Publisher's PDF, also known as Version of record

*Citation for published version (Harvard):*

Carter, L, Villapun, V, Grover, L & Cox, S 2022, 'Exploring the duality of powder adhesion and underlying surface roughness in laser powder bed fusion processed Ti-6Al-4V', *Journal of Manufacturing Processes*, vol. 81, pp. 14-26. <https://doi.org/10.1016/j.jmapro.2022.06.057>

[Link to publication on Research at Birmingham portal](#)

## General rights

Unless a licence is specified above, all rights (including copyright and moral rights) in this document are retained by the authors and/or the copyright holders. The express permission of the copyright holder must be obtained for any use of this material other than for purposes permitted by law.

- Users may freely distribute the URL that is used to identify this publication.
- Users may download and/or print one copy of the publication from the University of Birmingham research portal for the purpose of private study or non-commercial research.
- User may use extracts from the document in line with the concept of 'fair dealing' under the Copyright, Designs and Patents Act 1988 (?)
- Users may not further distribute the material nor use it for the purposes of commercial gain.

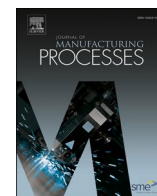
Where a licence is displayed above, please note the terms and conditions of the licence govern your use of this document.

When citing, please reference the published version.

## Take down policy

While the University of Birmingham exercises care and attention in making items available there are rare occasions when an item has been uploaded in error or has been deemed to be commercially or otherwise sensitive.

If you believe that this is the case for this document, please contact [UBIRA@lists.bham.ac.uk](mailto:UBIRA@lists.bham.ac.uk) providing details and we will remove access to the work immediately and investigate.



# Exploring the duality of powder adhesion and underlying surface roughness in laser powder bed fusion processed Ti-6Al-4V

Luke N. Carter<sup>\*</sup>, Victor M. Villapún, Liam Grover, Sophie C. Cox

Healthcare Technologies Institute, School of Chemical Engineering, University of Birmingham, Birmingham B15 2TT, UK

## ARTICLE INFO

### Keywords:

Laser powder bed fusion  
Surface roughness  
Image analysis  
Powder metallurgy  
Titanium alloys

## ABSTRACT

As-built surface roughness remains a significant barrier to widespread uptake of Laser Powder Bed Fusion (LPBF). To overcome this barrier, it is first necessary to understand the structure of this surface. This research explores the duality of the LPBF surface consisting of: 1) an apparent surface dominated by adhered powder and 2) the underlying profile defined by the fully consolidated material.

An array of cuboidal specimens were produced by LPBF with varying contour scan parameters to study their influence on the vertical wall surface. For the first time, optical image analysis was used to quantify the extent and size distribution of surface adhered powder particles. SEM micrographs of the sectioned specimens were used in conjunction with a second novel image processing technique to study the underlying surface profile. Researchers utilised these methods to study the relationship between process parameters and both surface topographies. These results were compared against traditional line of sight roughness measurements.

Surface finish ( $S_a$ ), powder adhesion, and underlying roughness decreased with energy input to a point where the contour melt track was observed as unstable and incoherent ( $\sim 0.1$  J/mm). A 19.9 % reduction in  $S_a$  was demonstrated by the smoothest specimen ( $S_a$ , 10.9  $\mu\text{m}$ ) when compared to the control ( $S_a$ , 13.6  $\mu\text{m}$ ). Argon crossflow within the process chamber was shown to influence the underlying roughness,  $R_a$ , with upstream values 4.0  $\mu\text{m}$  lower on average than downstream over most of the experimental range.

Adhered particle size showed a finer distribution compared with the feedstock ( $D_{50}$  Surface = 20.8  $\mu\text{m}$ ;  $D_{50}$  Feedstock = 32.9  $\mu\text{m}$ ). Consequently, a further study comparing specimens built using coarse (sieved to  $>36$   $\mu\text{m}$ ,  $D_{50}$  = 42.8  $\mu\text{m}$ ) versus fine (sieved to  $<36$   $\mu\text{m}$ ,  $D_{50}$  = 28.8  $\mu\text{m}$ ) powder was performed. Mean  $S_a$  for coarse powder specimens was 1.66  $\mu\text{m}$  greater than fine. However, coarse powder specimens showed fewer surface adhered particles due to geometric packing. Feedstock powder size fraction showed relatively little influence on underlying roughness.

Further discussion of particle adhesion mechanics is presented alongside practical processing implications. Finally, the authors suggest that continued research into the duality of the LPBF surface is necessary to not only improve the as-processed material, but to guide future development post-processing treatments.

## 1. Introduction

The battle to reduce surface roughness in Laser Powder Bed Fusion (LPBF) parts is critical in the path to widespread industrial adoption. As-built surfaces are typically unsuitable for mating components and have been shown to limit fatigue performance compared to traditional or machine finished parts [1–3]. The inherent attraction of Additive Manufacturing (AM) to produce patient specific medical implants is likewise limited by surface finish. A recent review by Lowther et al. [4] stated “surface finish and mechanical properties of parts in the ‘as-built’ state

can be significantly improved upon with appropriate post manufacture processing”. Cox et al. [5] demonstrated that surface adhered powder particles may limit the adhesion and migration of cells on Ti-6Al-4V samples produced by laser powder bed fusion (LPBF). Surface finish is therefore mechanically, functionally and, in the case of medical implants, biologically critical to the performance of the device.

Industrial practices for surface post-processing are often organisation or manufacturer specific (and sometimes closely guarded) but anecdotally may involve traditional tumbling or vibratory methods [6], media blasting, or hand polishing by skilled operators. Advanced

<sup>\*</sup> Corresponding author.

E-mail address: [L.N.Carter@bham.ac.uk](mailto:L.N.Carter@bham.ac.uk) (L.N. Carter).

<https://doi.org/10.1016/j.jmapro.2022.06.057>

Received 26 January 2022; Received in revised form 20 May 2022; Accepted 26 June 2022

Available online 1 July 2022

1526-6125/© 2022 The Authors. Published by Elsevier Ltd on behalf of The Society of Manufacturing Engineers. This is an open access article under the CC BY license (<http://creativecommons.org/licenses/by/4.0/>).

technologies including laser [7], chemical [8], abrasive flow machining [9], magnetic abrasive finishing [10], or hybrid methods have also been the subject of research [11], but are not currently widespread within industry. Regardless of how it is achieved, post-processing is often costly, labour intensive, and adds significant time to the overall supply chain. Additionally, they are incompatible with the idealised view that LPBF can produce complex internal features as most require access to the region being treated.

With these current practices in mind, the AM community as a whole must strive to improve as-built surfaces. Ideally the underlying technology will reach a point where post-processing is no longer required, that said even modest improvements at this stage would save time, improve accuracy and potentially energy consumption [12] by reducing post-processing material removal. The first step in achieving this is to understand the origins of as-built surface roughness, the mechanisms by which it forms, and underlying factors driving each of those mechanisms.

Disregarding the more complex issue of overhanging/supported surfaces, roughness of LPBF processed material is formed from a combination of three possible modes: top-surface roughness, stair-step roughness, powder adhered roughness.

Top-surface roughness relates solely to surfaces that lie parallel to the build plane and are formed by a single slice. Roughness here is formed due to the overlapping curvature of individual melt tracks as illustrated in Fig. 1(a). Several studies focus purely on the process refinement of this surface such as the research presented by Qiu et al. [13] regarding palladium modified titanium alloys and Hong et al. [14] relating to cobalt-chrome. The former showed that top-surface roughness increases with increasing laser speed (a decreased overall energy input) due to increased curvature of the melt pool, a finding that was confirmed by Zhang et al. [15] for Ti-6Al-4V. The latter showed that there is an optimum scan-spacing for minimum top surface roughness, again relating to the geometry of the track. A further study by Yasa et al. [16] demonstrated the possibility to improve the top surface roughness of both LPBF formed Ti-6Al-4V and 316L steel using laser surface remelting. Whilst these studies are interesting from a process understanding point-of-view, they provide little practical use as in most cases the fraction of a component's surface that forms a perfect top-surface plane is limited.

Roughness of the side walls is greater than that of the top-surface as noted in the review by Frazier [17]. Mumtaz & Hopkinson [18] and Krol & Taski [19] also noted greater side wall roughness in their studies of IN625 and Ti-6Al-4V respectively. For most real-world components, relatively few surfaces will lie perfectly horizontal ( $\alpha = 0^\circ$ ) making studies focussing purely on the top-surface of limited practical value. For

this majority of non-horizontal surfaces, the roughness is mainly driven by some combination of both the stair-step and powder adhered mechanisms. Strano et al. [20] reported the relationship between increasing wall angle and increased surface adhered 316 L powder particles in 2013. Subsequently it was also reported in the surface optimisation work by Leary [21] and the predictive toolset proposed by Villapún et al. [22]. Given the nature of the LPBF process, this relationship is almost implicit. Assuming that the majority of powder particles adhere to the surface where loose power is in contact with molten/hot material, i.e. on the outer edge of contour scan track. Simple geometry shows that these regions make up a greater proportion of the outer wall as the build angle increases [10]. Fig. 1(a–c) illustrates this relationship with increasing build angle. By contrast, trends reported by Vandenbroucke & Kruth [23] and Villapún et al. [22] both showed the inverse relationship between sloping angle and the stair-step roughness. It can therefore be suggested that at lower angles surface roughness is driven by the stair-step effect but as the build angle approaches vertical, powder adhered roughness becomes dominant. This is further supported in a study by Spierings et al. [24] who demonstrates that vertical surface roughness decreases with particle size in LPBF processed 316 steel.

Despite the extent of the powder adhered roughness on outer surfaces, there have been relatively few investigations into the subject with even simple LPBF parameter/roughness relationships for vertical surfaces being scarce in literature. Abele & Kniepkamp [25] show an increase in side wall roughness of LPBF processed 316 L steel under low line energy ( $<75$  mJ/mm) conditions where the melt track has been observed to be unstable, although the study is limited to this extreme of processing. A more general trend showing a decrease in side surface roughness with increasing laser speed (i.e. decreasing energy input) for LPBF of Ti-6Al-4V is presented by Zhang et al. [15]. This same general trend is weakly apparent in research of Cozzolino et al. [12] who also remark that it is an interplay of multiple roughness mechanisms that may be obscuring strong correlations.

Lack of understanding in this area is further demonstrated in the language used regarding the surface adhered powder particles with some investigators referring to 'partial melting' [19,21,23,25–28], 'sintering' [26], simply 'adhesion' [20,29,30], and occasionally 'balling' [15,18]. At least part of the reason for this are the limitations of traditional surface measurement techniques when presented with the vertical wall LPBF surface. Both optical and tactile systems use line-of-sight methods which fail to quantify the overhangs and regions 'hidden' by the attached particles. Diaz et al. [26] suggest the concept of both primary (underlying) and secondary (powder-adhered) roughness and show finishing methods targeting the removal of the latter often fail to produce the expected numerical improvements in roughness

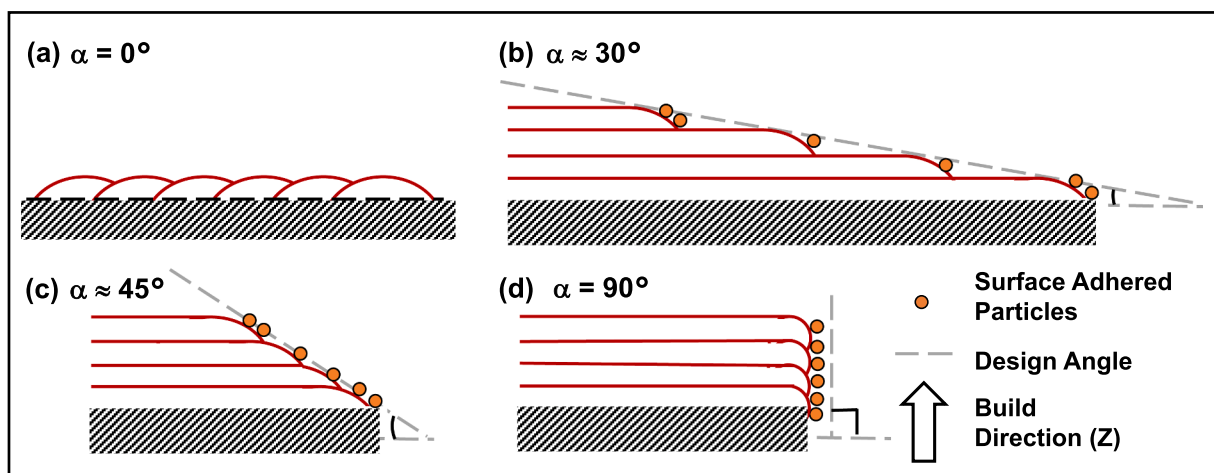


Fig. 1. Diagram illustrating the changing importance of surface roughness modes with increasing build angle during LPBF; (a)  $0^\circ$ , (b)  $30^\circ$ , (c)  $45^\circ$ , (d)  $90^\circ$ .

measurements as they simply reveal the underlying surface. Similarly, the study by Triantaphyllou et al. [27] recognises the limitations of traditional methods in characterising the LPBF surface and compares results against a destructive surface roughness measurement utilising image analysis and microscopy.

Surface roughness presents a significant barrier to the wider uptake of AM as a manufacturing method. Greater understanding of the powder adhesion and underlying contributions to LPBF surface roughness will be necessary before processing and subsequent post-processing techniques can be optimised and improved. Using a combination of traditional and novel image analysis techniques, this research presents an exploration of the fundamental influence of LPBF contour process parameters and particle size distribution on powder adhered and underlying roughness with respect to vertical surfaces of Ti-6Al-4V cuboidal coupons.

## 2. Methods

### 2.1. Specimen manufacture

10 mm cuboidal specimens were produced using a RenAM500M laser powder bed fusion system (Renishaw, UK) equipped with a 1080 nm ytterbium laser focussed to a spot diameter of 80 µm at the powder bed. For specimens produced using sieved powder, a Reduced Build Volume (RBV) modification was installed to allow for the smaller volume of available powder. A hatch fill and single outer contour laser scanning strategy was utilised with beam compensation (distance between the design geometry edge and contour scan path) and hatch offset (distance between contour scan path and hatch region) fixed at 95 µm and 40 µm respectively; these offsets ensure that the vertical wall surface of the specimens is produced by the cumulative edges of the contour scan only. Given the RenAM500M's modulated method of laser control, whereby laser path is defined as a series of points each with a specified dwell time, point distance was fixed at 90 µm and laser speed was varied using the point dwell as shown in Eq. (1):

$$v = \frac{d}{t} \times 1000 \quad (1)$$

where  $v$  is laser speed, mm/s,  $d$  is point distance, µm, and  $t$  is point dwell, µs.

In order to study purely the contour processing parameters' influence on the vertical wall surface, the hatch region of all specimens were assigned standard Ti-6Al-4V processing parameters (200 W laser power, 60 µs point dwell, 90 µm point distance). Likewise, all specimens were offset from the build substrate by 3 mm using standard pin supports, assigned a 30 µm layer thickness, and were built in an array located in the central portion of the build plate in order to reduce unintended variability due to plate location. Processing was performed under Ar atmosphere at atmospheric pressure, recirculated via a filter at 180 m<sup>3</sup>/h.

A single contour strategy was selected to study the fundamental parameter/surface relationship as preliminary work indicated that multiple contour, as often used in LPBF processing, introduced uncontrollable variability from alternating directions and unpredictable start/end points. Three batches of specimens were produced, each using different powder feedstock: as-supplied Ti-6Al-4V (15–53 µm); coarse (>36 µm sieved) Ti-6Al-4V, fine (<36 µm sieved) Ti-6Al-4V. Contour processing parameters, feedstock, system configuration, and line energy (Laser Power (W)/Laser Speed (mm/s), J/mm) for each specimen are shown in Table 1. A control specimen was also built using standard in-house parameters for processing of Ti-6Al-4V (200 W laser power, 60 µs point dwell, 4 contours with 90 µm spacing).

**Table 1**

Contour laser parameters for all specimens.

Powder	Laser power (W)	Point dwell (µs)	Laser speed (mm/s)	Line energy (J/mm)	
As-Supplied	150	180	500	0.3	Full substrate
		90	1000	0.15	
		60	1500	0.1	
		45	2000	0.075	
		36	2500	0.06	
	200	180	500	0.4	
		90	1000	0.2	
		60	1500	0.1333	
		45	2000	0.1	
		36	2500	0.08	
	250	180	500	0.5	
		90	1000	0.25	
		60	1500	0.1666	
		45	2000	0.125	
		36	2500	0.1	
	300	180	500	0.6	
		90	1000	0.3	
		60	1500	0.2	
		45	2000	0.15	
		36	2500	0.12	
Fine (<36 µm)	Control 200	Control 180	Control 500	Control 0.4	RBV
		90	1000	0.2	
		60	1500	0.1333	
		45	2000	0.1	
		36	2500	0.08	
Coarse (>36 µm)	200	180	500	0.4	
		90	1000	0.2	
		60	1500	0.1333	
		45	2000	0.1	
		36	2500	0.08	

### 2.2. Powder feedstock

Plasma atomised Ti-6Al-4V (Grade 23, composition provided in Table 2) Powder feedstock was supplied by Carpenter Additive (Carpenter Technology Corporation, US) in the size range 15–53 µm as typical for LPBF processing. A small volume of powder was manually sieved to 36 µm under argon atmosphere to create a coarse (>36 µm) and fine (<36 µm) fraction. Particle size distribution was confirmed for all three powders by an external test laboratory using laser diffraction (Mastersizer 2000, Malvern Instruments, UK). Particle size distribution is provided in Fig. 2(a) alongside D<sub>10</sub>, D<sub>50</sub>, and D<sub>90</sub> values.

### 2.3. Specimen preparation

Following debuild, the plate was water jet washed to release loose powder. Specimens were removed from the build substrate carefully using hand tools to avoid damaging the vertical walls and were individually cleaned in an ultrasonic bath of isopropanol for 15 min each to ensure that loose powder particles had been removed from the surface. Following vertical wall surface measurement and top surface microscopy, specimens were sectioned along the midplane (X-Z) using wire electro-discharge machining as shown in Fig. 2(b). For further SEM imaging of the surface profile specimens were hot mounted in conductive Bakelite, sequentially ground from 250 to 4000 grit, before final polishing with activated colloidal silica using standard metallurgical techniques.

**Table 2**

Ti-6Al-4V (Grade 23) powder composition (%wt.) as provided by manufacturer.

Ti	Al	V	O	N	H
Bal.	6.4 (wt%)	4.0 (wt%)	0.11 (wt%)	0.01 (wt%)	0.003 (wt%)

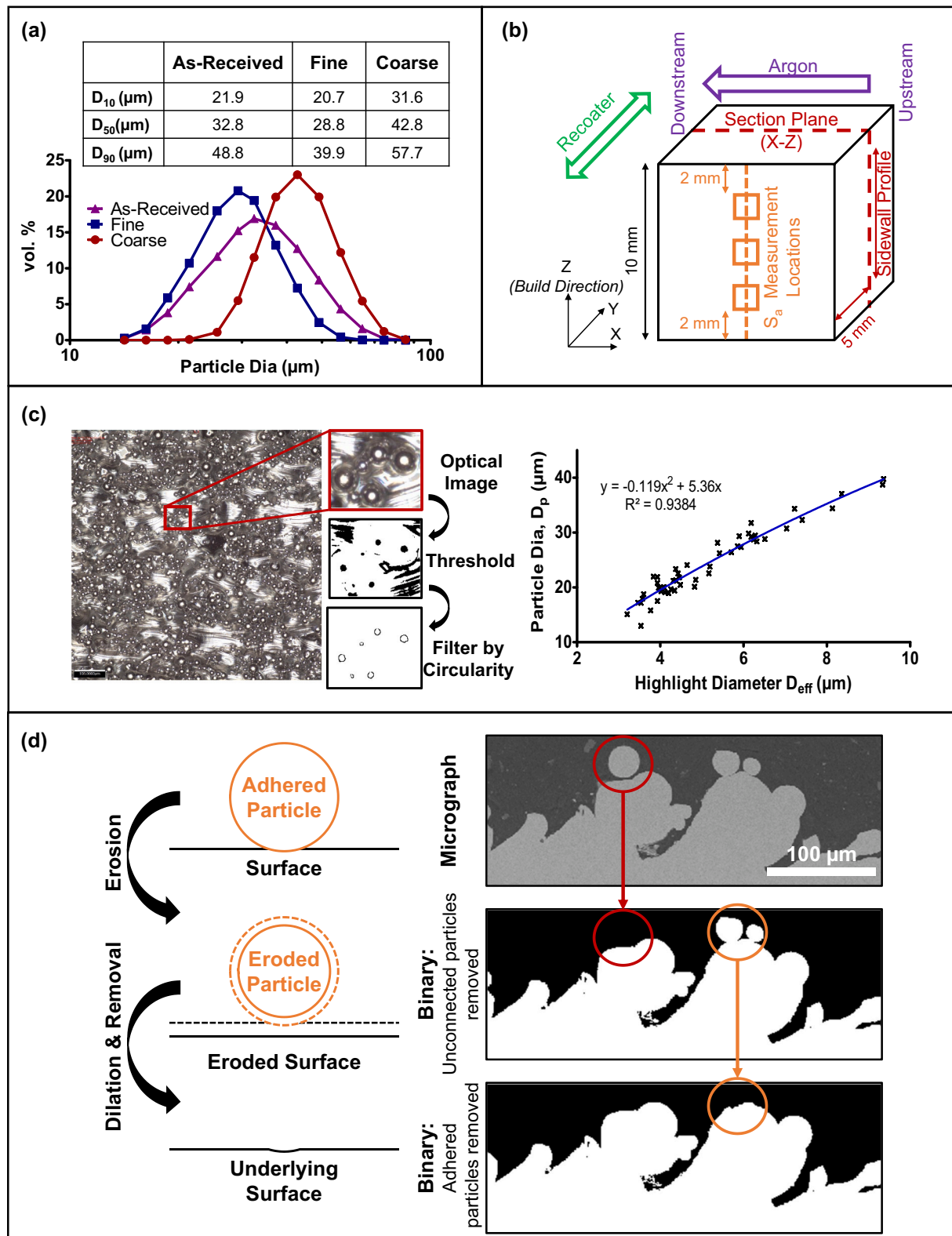


**Fig. 2.** Method details: (a) Powder size distribution for as-received and two sieved fractions (Coarse & Fine). Inset table shows  $D_{10}$ ,  $D_{50}$ , and  $D_{90}$  values; (b) Specimen details indicating orientation, measurement locations, section plane, and relative direction of argon crossflow; (c) Example illustrating image analysis procedure to identify surface adhered particles alongside calibration curve from effective highlight diameter to particle diameter; (d) Schematic representation showing how the bespoke MATLAB function identifies and removes surface adhered particles from profile micrograph alongside example images for each step.



## 2.4. Surface roughness measurement

Surface roughness, arithmetical mean height of surface ( $S_a$ ), measurements were taken with an Alicona InfiniteFocus (Bruker, US) system using  $20\times$  objective lens to give an area of  $812 \times 812 \mu\text{m}$  for each region. Cutoff wavelength,  $\lambda_c$ , was set to the system maximum,  $406 \mu\text{m}$ , to capture all roughness contributors with no further filtering applied. Three regions were measured on the same X-Z side wall of each specimen positioned along the vertical midline of the face with the upper and lower measurements being 2 mm from the top and bottom surface of the specimen as shown in Fig. 2(b). Special care was taken to ensure that same relative face and positions were measured on each specimen to avoid the influence of corners or bed orientation. Composite focus optical images were collected alongside the  $S_a$  data for further image analysis.

## 2.5. Surface adhered particle image analysis

A novel image analysis approach was developed to mitigate the challenge of tightly packed and partially overlapping particles in order to quantify the number and size of the surface adhered particles from the optical images. Rather than attempt to differentiate the particles, a bespoke ImageJ [31] macro was created to threshold the reflected highlights on the metal surface due to microscope illumination. Detected particles were then filtered by circularity (0.7–1.0) corresponding to reflections on a spherical powder particle surface as illustrated in Fig. 2(c) and the area of each highlight recorded. Assuming perfectly spherical powder particles and uniform collimated illumination, the highlight diameter will be proportional to the particle diameter. The diameter of 50 clearly visible particles were manually measured using ImageJ and plotted against effective highlight diameter,  $D_{\text{eff}}$  ( $\mu\text{m}^2$ ), as shown in Eq. (2):

$$D_{\text{eff}} = 2\sqrt{A/\pi} \quad (2)$$

where  $A$  is the highlight area in  $\mu\text{m}^2$ . Fig. 2(c) shows the relationship between the effective highlight diameter and the measured diameter of each particle. A least-squares 2nd order polynomial provided the best fit to the data with  $R^2 = 0.94$  and a standard error of estimate,  $\sigma_{\text{est}}$ , of  $1.55 \mu\text{m}$  between the measured and predicted values. Despite the assumptions, this method of using the highlight area to estimate the particle size appears to be reasonable. It also allows for the automated quantification and measurement of the several thousand particles visible on the surface whilst overcoming some of the challenge of overlapping/closely adjacent particles. Adhered particle diameter,  $D_p$  ( $\mu\text{m}$ ), was therefore estimated from highlight area for all optical images using Eq. (3):

$$D_p = 5.36D_{\text{eff}} - 0.119D_{\text{eff}}^2 \quad (3)$$

## 2.6. Microscopy

Microscopy was performed using a TM3000 (Hitachi, Japan) benchtop SEM fitted with BSE detector. Micrographs of the top (X-Y) surface for each specimen were taken at several magnifications between  $50\times$  and  $500\times$  showing the final layer contour scan track. This was to provide qualitative characterisation of the uniformity and stability of the contour laser scan track.

Sectioned (X-Z) samples were used to study the side wall (Y-Z) profile. A series of 9 sequential micrographs were collected from each side wall profile starting at 2 mm below the top surface at  $200\times$  magnification. Each set were manually stitched together to show an approximately 6 mm length of sidewall profile for both the argon crossflow upstream and downstream surfaces of specimens as shown in Fig. 2(b).

## 2.7. Sectioned profile image analysis

A Bespoke MATLAB [32] function was created to evaluate the underlying roughness (i.e. without the influence of adhered powder particles) from the stitched side wall micrographs. Code is available upon reasonable request to the authors and the function logic is as follows. A threshold is applied to the micrograph producing a binary image separating the metal from the surrounding Bakelite. All unconnected particles and image noise are removed to leave only the surface; this removes many of the surface adhered particles as only those where the micrograph section passes through the neck connecting the particle to the surface appear connected when viewing a 2D plane.

To remove the particles visibly connected to the surface, the thresholded image is eroded by one pixel at a time for up to six erosions. As particles are typically attached by a 'neck' region much narrower than their diameter these erosions separate the particles from the underlying surface. Following each erosion any regions that have become detached from the surface are evaluated for circularity. Those showing a circularity  $>0.7$  can be considered as powder particles. These regions are re-dilated by as many pixels as they were eroded and removed from the initial thresholded image to form the surface without the adhered particles. This is represented schematically in Fig. 2(d) alongside example images of the process on a small section of a typical profile.

A simple despeckle filter is applied before the profile is extracted from the binary image and an overall correction applied to accommodate any minor angular misalignment present in the micrographs. Finally the surface roughness, arithmetical mean height of line ( $R_a$ ), is calculated for the resulting underlying profile using the common digital form shown in Eq. (4):

$$R_a = \frac{\sum |Z_i|}{N} \quad (4)$$

where  $Z$  ( $\mu\text{m}$ ) is the deviation from mean surface height, and  $N$  is the number of uniformly spaced  $Z$  values.

## 2.8. Statistical analysis

Standard two-way ANOVA was performed on surface roughness, surface adhered particle count, and underlying roughness datasets to investigate the significance of each process variable.

## 3. Results & discussion

### 3.1. Surface roughness, $S_a$ As-received powder

Fig. 3(a) shows the relationship between LPBF contour process parameters and surface roughness,  $S_a$ , of the specimen side wall. In general  $S_a$  decreases with increasing scan speed reaching minimum values in the range of  $10.9$  to  $12.1 \mu\text{m}$ . These lie below the mean  $S_a$  for the control Ti-6Al-4V parameters,  $13.6 \mu\text{m}$ , showing a maximum reduction of  $19.9\%$  and suggesting that even a simple parameter study may yield positive improvement to as-built surfaces. Less obvious is the trend showing surface roughness decrease when reducing laser power. This is most notable at the slowest scan speed ( $500 \text{ mm/s}$ ) where the mean  $S_a$  value for  $300 \text{ W}$  power is  $3.6 \mu\text{m}$  ( $21.1\%$ ) greater than the  $150 \text{ W}$  roughness.

From the results in Fig. 3(a) it might be suggested that surface roughness is driven purely by the combined power and speed parameter, line energy ( $\text{J/mm}$ ), however the plot in Fig. 3(b) showing the same  $S_a$  values against line energy reveals a more complicated relationship. In general roughness increases with line energy as expected given that it decreases with scan speed. However, equivalent line energy specimens show different surface roughness values with the lower power conditions generally giving greater  $S_a$  values than higher power for the same line energy. For example,  $150 \text{ W}$ ,  $1500 \text{ mm/s}$  and  $250 \text{ W}$ ,  $2500 \text{ mm/s}$  specimens both have a line energy of  $0.1 \text{ J/mm}$ , however their mean  $S_a$

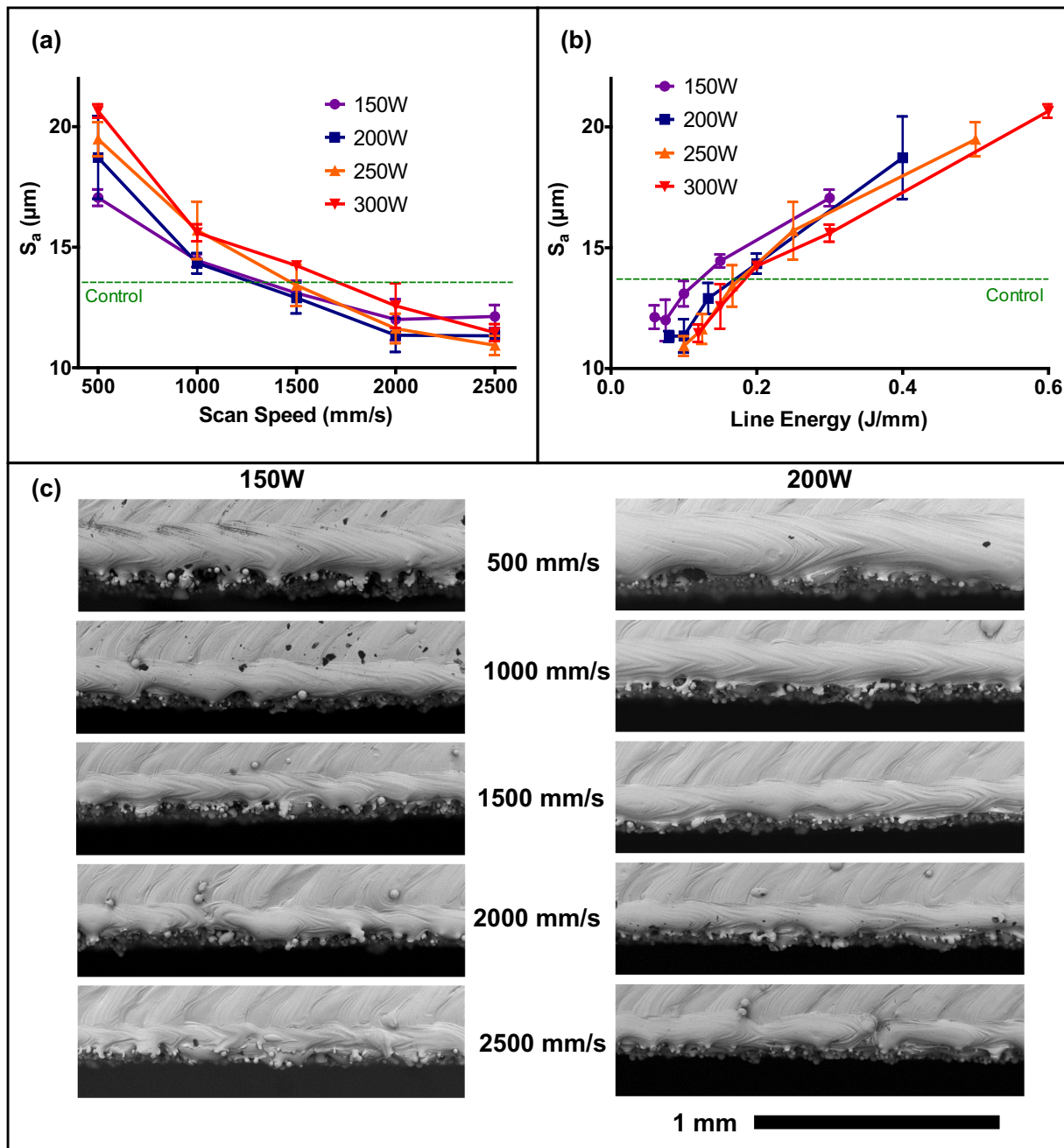


**Fig. 3.** Plots showing mean  $S_a$  values for specimens produced using as-received powder for each laser power against (a) scan speed and (b) line energy; error bars show  $\pm\sigma$  of the three measurement regions. Green dashed line indicates mean roughness from the control parameters used for Ti-6Al-4V (c) Shows top-surface micrographs of the outer contour for 150 W and 200 W specimens over increasing scan speeds. (For interpretation of the references to colour in this figure legend, the reader is referred to the web version of this article.)

values are 13.1 μm and 10.9 μm respectively. This lies contrary to what might be assumed given the individual parameter relationships and suggests a more nuanced role for each parameter.

A two-way ANOVA performed on this dataset produced  $P$  values  $<0.0001$  for both the power and the scan speed parameters suggesting both have an extremely significant effect on  $S_a$ . Scan speed was found to account for 89.4 % of the variance seen in the results compared to 2.8 % for power, confirming the observation that  $S_a$  is driven significantly by scan speed within this experimental range (500–2500 mm/s). Interaction between the two parameters produced a  $P$  value = 0.0025, still considered very significant, and accounting for 3.9 % of the variance observed.

One further point to note is the levelling then slight increase in  $S_a$

values for both 150 W and 200 W datasets at faster scan speeds between 2000 mm/s and 2500 mm/s shown in Fig. 3(a). The cause is revealed in SEM micrographs of the contour taken from the sample top surface as shown in Fig. 3(c). Whilst the contours of almost all specimens appear uniform in width, continuous, and stable; those for both 150 W and 200 W become irregular and partially broken at high scan speeds (2000 mm/s and 2500 mm/s). As the side wall is made up of multiple contour scan tracks, it is easy to imagine that under these low energy conditions the irregularity and discontinuity make their own significant contribution to surface roughness which lies counter to the parametric relationships observed under stable conditions.

These  $S_a$  results are further supported by published research. Zhang et al. [15] show a similar overall trend of decreasing roughness with

increasing scan speed. Whilst Abele & Kniepkamp [25] report an increase in surface roughness under low energy conditions where the melt-track was observed to be unstable. Although interesting and useful from a practical processing viewpoint,  $S_a$  as a simple numerical value, reveals little information as to the contribution of adhered powder or the underlying profile to the surface. This, alongside the limitations of profilometry, highlights the need for less conventional analysis techniques to uncover the relationship between powder adhesion and underlying contributions to LPBF surface roughness.

### 3.2. Particle image analysis, As-received powder

Using the novel image analysis technique outlined in Section 2.5 it was possible to quantify the particles adhered to the surface along with an estimate of their size distribution. Fig. 4(a) shows the number of surface adhered particles identified per  $\text{mm}^2$ . The overall trend agrees with that of the surface roughness showing an increase in laser scan speed decreases the quantity of surface adhered particles. This suggests that a lower energy input results in reduced surface particle adhesion and consequently lower overall roughness. A qualitative examination of

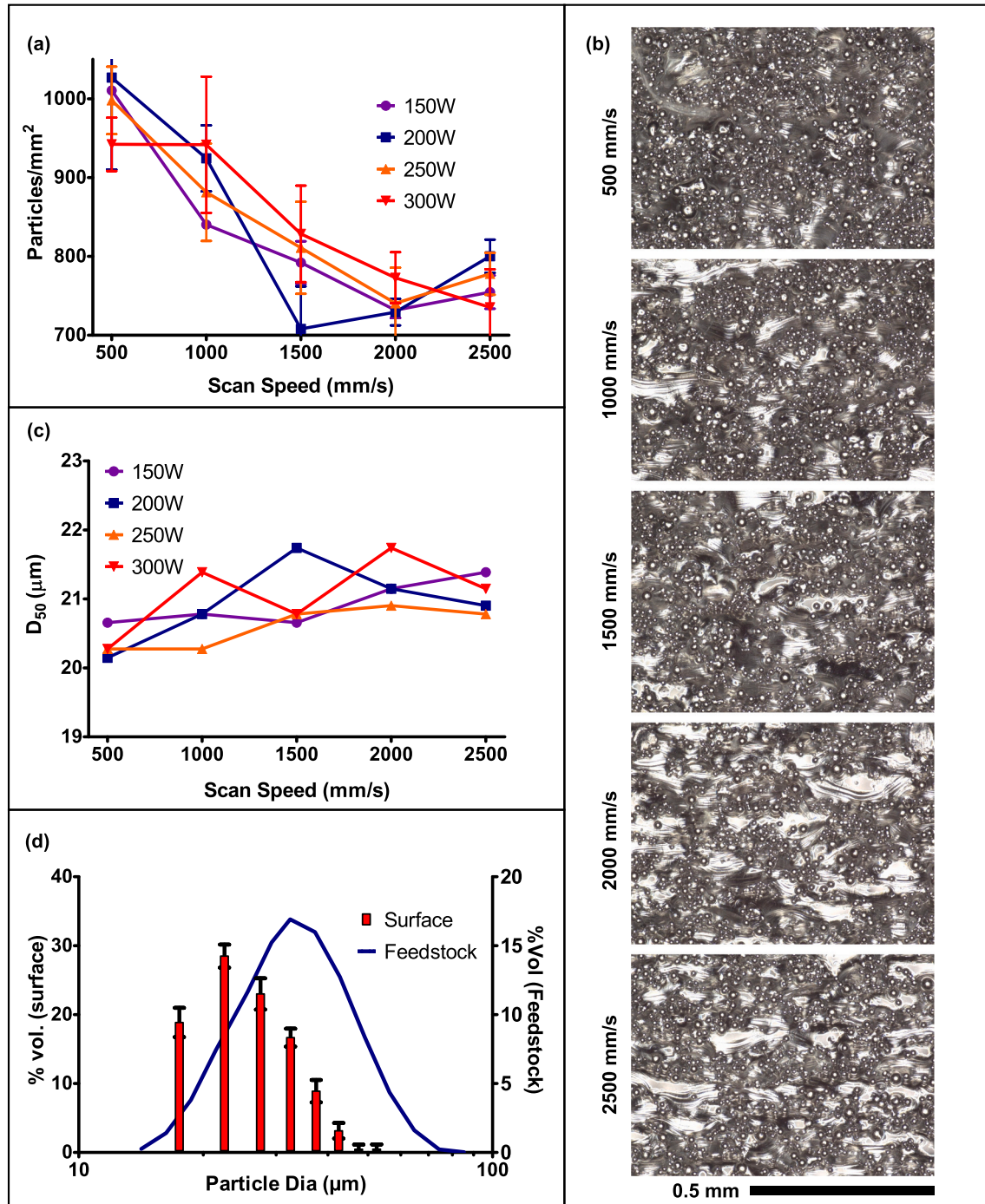


Fig. 4. Surface adhered particle image analysis results. (a) Plot showing number of particles/ $\text{mm}^2$ ; error bars show  $\pm\sigma$  based on the three measurements. (b) Typical optical composite focus micrographs for 250 W with increasing scan speed. (c) Plot showing  $D_{50}$  values for each specimen calculated from surface adhered powder analysis. (d) Mean particle size distribution of surface adhered powder (red columns) compared to the feedstock powder (blue curve). (For interpretation of the references to colour in this figure legend, the reader is referred to the web version of this article.)



the source micrographs further supports this; Fig. 4(b) shows typical images from the surface of the 250 W specimens. As scan speed increases the number of adhered particles clearly decreases revealing more of the underlying surface.

2500 mm/s specimens for powers 150 W and 200 W show a slight increase in surface adhered particles compared to the 2000 mm/s specimens. A similar marginal increase is observed in the mean value of the 250 W specimens for 2000 mm/s and 2500 mm/s, however these values lie within  $\pm\sigma$  of each other and so should be treated cautiously. This also reflects the trend observed in the surface roughness measurements shown in Fig. 3(a). Examination of the micrographs fails to fully explain this result, however it could be suggested that as underlying roughness increases due to melt track instability at low energy conditions, as discussed in Section 3.1, more loose powder is trapped on the surface by the irregular underlying morphology.

It should be noted that the standard deviation of particle count for each specimen is relatively large as seen in the error bars of Fig. 4(a). In part this is likely due to variability in the technique resulting from the circularity method of filtering particles. Some smaller particles may not be identified correctly, likewise some incidental reflections from the underlying surface may meet the criteria to be identified as a particle. Performing measurements over a wider area would improve confidence in the data however, as noted in Section 2.4, only the midline of the specimen on a specific face could be used to ensure minimal unintended variability. Despite this, a two-way ANOVA revealed a  $P$  value  $<0.0001$  for scan speed suggesting it is an extremely significant factor accounting for 69.0 % of the observed variability. Both laser power and the interaction between power and speed were both shown to be non-significant producing  $P$  values of 0.88 and 0.30 respectively. Given that power was shown to be significant in the surface roughness analysis, but accounted for a much lower proportion of the observed variability, it may be that a similar relationship exists relating to adhered particles but is unobservable within this dataset due to the high degree of experimental scatter. This novel image analysis method further aids in understanding the surface roughness. Correlation between the trends in adhered particles and overall surface roughness measurements confirm the hypothesis that powder adhesion is the key mechanism driving surface roughness for these vertical wall specimens.

Using the geometric relationship (Eq. (3)) between the highlight and particle diameters it was possible to estimate the size of each particle identified on the surface. By further calculating the effective volume of each particle and binning the data, an approximate particle size distribution was produced.  $D_{50}$  values of the surface adhered powder for each specimen are presented in Fig. 4(c). The data shows no clear trend with contour process parameters. Alongside examination of each individual sample distributions, this confirms that the size distribution of surface adhered powder is relatively constant across all specimens within the parameter range investigated. Fig. 4(d) compares the mean surface adhered particle size distribution for all specimens with that of the feedstock powder. Here the distribution peak for the feedstock represents a larger particle size than that of the surface adhered powder with  $D_{50}$  values of 32.9  $\mu\text{m}$  and 20.8  $\mu\text{m}$  respectively. Of course, a certain amount of caution should be taken when interpreting these results. Accuracy of the image analysis method limits its application to particles with diameter  $>15 \mu\text{m}$  due to the image resolution needed to correctly resolve and identify the reflection highlights. Nevertheless, it does suggest preferential adhesion of finer particles to the surface when compared to the feedstock material.

### 3.3. Underlying surface roughness, As-received powder

Image analysis of stitched SEM micrographs were used to measure the underlying (i.e. with adhered particle removal) roughness,  $R_a$ , of each specimen. As before, measurements were carried out along the midline of the specimen to avoid corner effects for both upstream and downstream surfaces with respect to the argon crossflow in the process

chamber. Mean underlying  $R_a$  values calculated from both surfaces for each specimen are shown in Fig. 5(a). Underlying  $R_a$  decreases with increasing laser scan speed and decreasing power; in short the trend aligns with those seen previously where roughness decreases with energy input (Figs. 3(a) and 4(a)). Two-way ANOVA shows that both power and speed are significant factors with  $P$ -values of 0.0002 and  $<0.0001$  respectively. From fundamental principles of the process, it is understood that increased energy input increases the melt pool size in both width and depth. Consequently the corresponding stair-step undulations will likewise increase in amplitude producing a rougher underlying surface.

Comparing upstream and downstream roughness for each specimen reveals a secondary interesting trend shown in Fig. 5(b). The general trend holds for each type of surface, however downstream surfaces almost universally show a greater  $R_a$  value than the corresponding upstream surface on the same specimen. For laser powers in the range 200 W to 300 W and for speeds  $<2500$  mm/s, downstream  $R_a$  is between 2.3 and 6.7  $\mu\text{m}$  greater than the upstream surface with the mean difference being 4.0  $\mu\text{m}$ . Under lower energies  $R_a$  values for each surface are more similar as seen in the 150 W specimens and all specimens corresponding to 2500 mm/s laser scan speed. SEM micrographs in Fig. 5(c) show a section of each surface for the 250 W specimens providing a qualitative confirmation of this result. Each downstream surface appears notably more irregular than the corresponding upstream surface, a difference that is more apparent under slow laser scan speeds.

In an effort to improve part quality, LPBF system manufacturers have moved towards higher gas flow rates to draw away uncontrolled spatter and material condensate [33] which are known to be detrimental to component quality [34]. In this case however the greater inert gas flowrate may also have produced an orientation inhomogeneity in the vertical wall roughness. From examination of the surface profiles it appears as though the contour tracks are distorted in the direction of the crossflow due to the aerodynamic drag of the gas on the liquid melt pool. In turn this has increased the measured roughness, an effect that only becomes more apparent with increased energy and corresponding increase in melt pool size [15]. Investigation of this phenomena, experimentally or computationally, is highly challenging due to the irregular surface, surrounding powder, high thermal gradients, phase changes, and local gas flow characteristics. Detailed investigation of Ar crossflow influence on the melt pool geometry therefore remains a topic outside the scope of this research and a matter for future study. Numerical analysis of the deformation of a droplet on a flat surface in a fluid flow [35] provides some support for this hypothesis, albeit in a greatly simplified scenario. In general terms, the relative deformation of a droplet depends on flow velocity given constant dynamic viscosity and surface tension and that absolute deformation values will increase with droplet size.

Study of the underlying surface has revealed similar trends to that of surface powder adhesion. Additionally, a secondary influence on surface roughness has been identified that shows a difference between upstream and downstream vertical walls with respect to the argon crossflow during processing. This is an interesting result in itself warranting future investigation and highlights the difficulty of isolating individual factors driving surface roughness formation.

### 3.4. Sieved powder

In order to better understand the influence on the feedstock particle size similar experiments were repeated with fine and coarse fractions of powder obtained via hand sieving. Specimens were produced using a fixed 200 W contour laser power and the RBV auxiliary unit due to the limited material available in these fractions. Whilst practically necessary, it should be noted that the RBV assembly slightly alters the process plane height, crossflow within the chamber, and the method of powder dosing. Given the sensitivity of surface roughness to unintended influences comparison between these results and those of the as-received

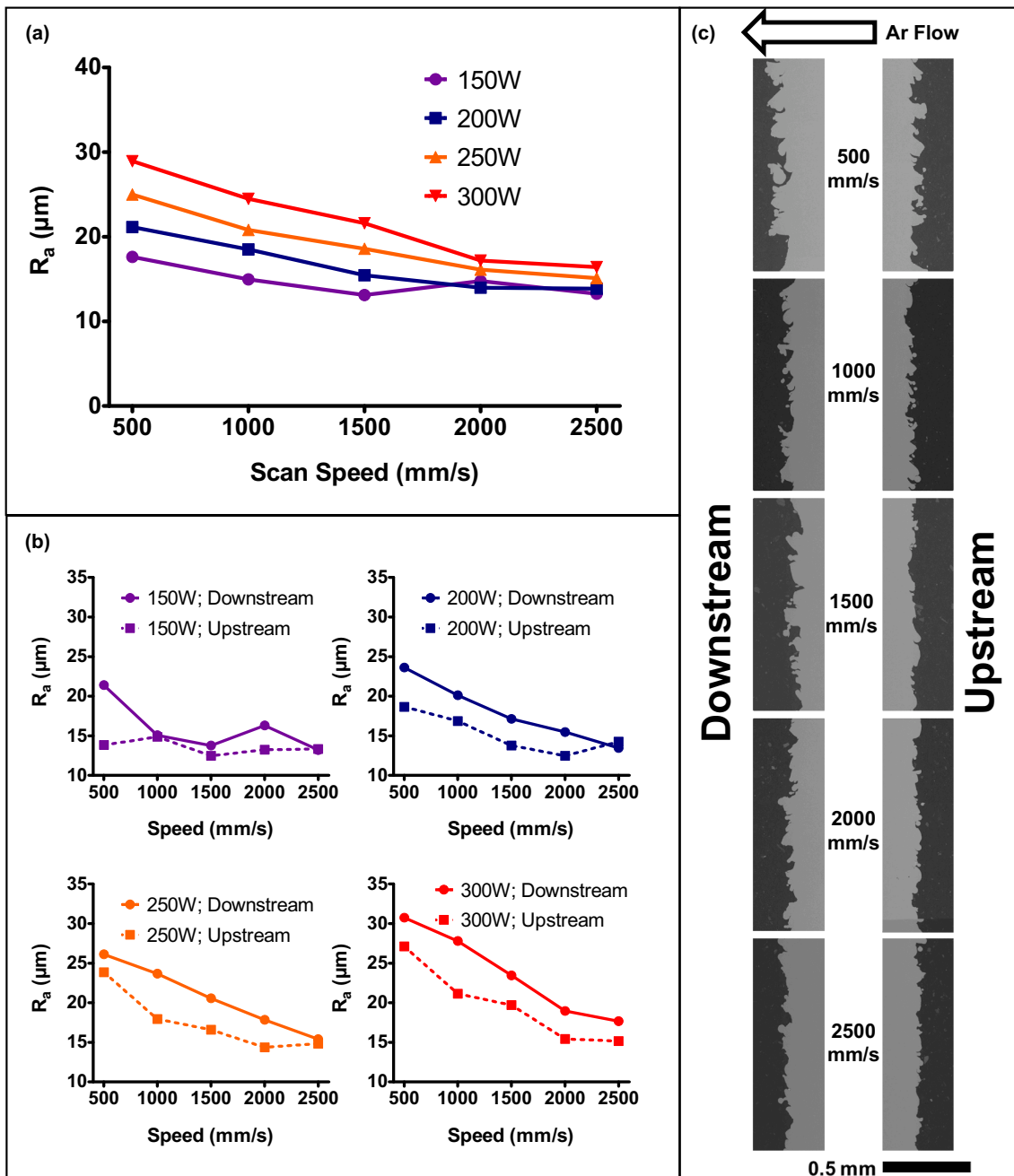


**Fig. 5.** Underlying surface roughness of vertical walls produced using as-received feedstock. (a) Mean underlying  $R_a$  against laser scan speed for different laser powers. (b) Underlying  $R_a$  for upstream and downstream surfaces for each laser power. (c) BSE SEM micrographs showing sections of 250 W surfaces both upstream and downstream in the Ar crossflow.

powder should be limited to the trends only.

Overall  $S_a$  variation with laser scan speed for fine and coarse fractions is shown in Fig. 6(a). The same general trend as seen with the as-received powder (Fig. 3(a)) can be seen in both fractions with roughness initially decreasing with laser scan speed before increasing slightly. One notable difference is that the minimum  $S_a$  value appears to plateau before rising again. However, given that both fine and coarse results show approximately the same shape of curve however it can be assumed that this difference is due to the use of the RBV.

The most distinctive feature of Fig. 6(a) however is that, despite following a similar trend, the coarse powder produces a reliably rougher surface than the fine for the same processing parameters. On average coarse powder produced an  $S_a$  of 1.66  $\mu\text{m}$  greater (10.3 %) than that of the fine. This is unsurprising given that surface adhered powder is a key

driving force of vertical wall roughness and, as  $S_a$  is a measure of mean surface deviation, it is expected that larger particles would produce a rougher surface. Spierings et al. [24] previously reported the same trend regarding 316 L steel. What is surprising is that the difference in  $S_a$  is so small between the size fractions; from feedstock analysis  $D_{50}$  is 14  $\mu\text{m}$  greater for the coarse powder, yet only produces an  $S_a$  increase of 1.66  $\mu\text{m}$ . Such a comparatively small difference in roughness highlights the limitations of traditional profilometry measurement techniques when examining this type of surface. The ALICONA system only measures the visible surface which, in this case, is largely made up of adhered particles. By measuring this 'false' upper surface formed from the visible regions of adhered spherical particles the diameter for those particles has less influence than may be expected. Measurement limitations when dealing with this type of complex surface are also recognised in the

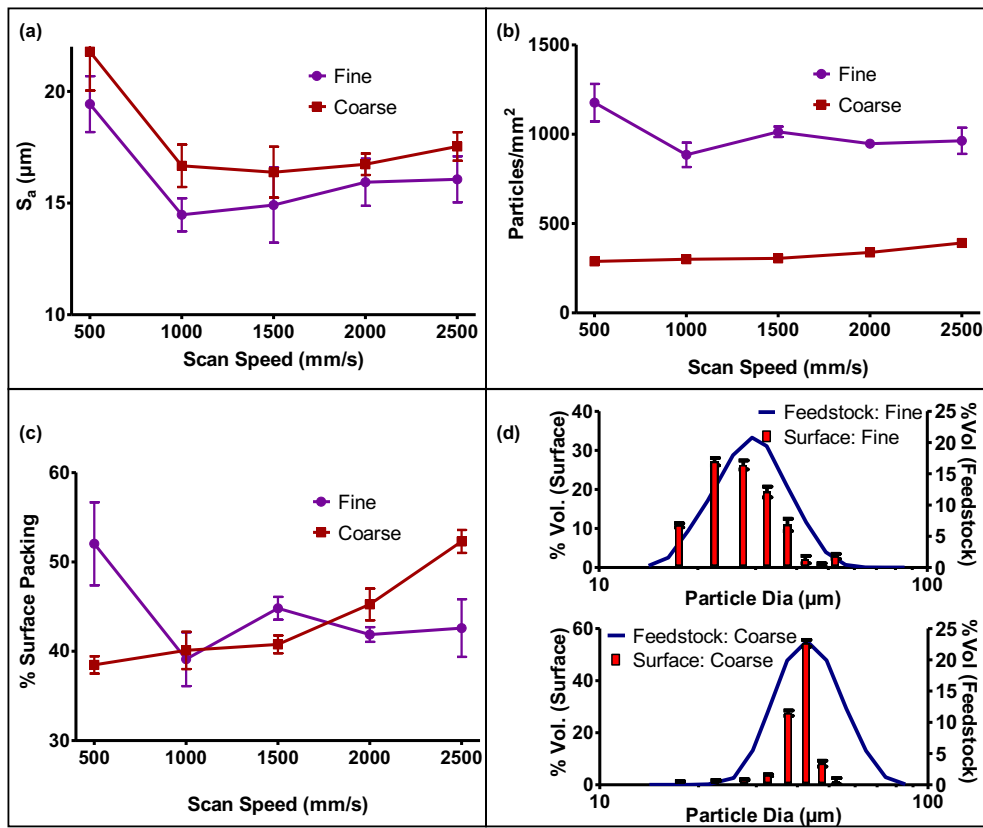


**Fig. 6.** Roughness results for both fine ( $<36 \mu\text{m}$ ) and coarse ( $>36 \mu\text{m}$ ) powder fractions process at 200 W contour laser power. Plots showing (a)  $S_a$  against laser speed; (b) surface adhered particles per  $\text{mm}^2$  against laser scan speed; (c) surface adhered particles normalised as a % of maximum theoretical 2D packing; (d) comparison between the surface measured particle size distribution and analysis of feedstock powder.

papers by Triantaphyllou et al. [27] and Diaz et al. [26].

Surface adhered particles per  $\text{mm}^2$  (Fig. 6(b)) is dramatically different between the powder fractions with values on average 3 times greater for fine powder than coarse. However, these measurements fail to account for differences in number of particles in contact with the side wall/edge of melt pool during processing. An approximate estimate of the maximum number of particles in a plane can be made by assuming perfect hexagonal close packing (HCP) of monosize circles. In this case, HCP has been proven to be the most efficient arrangement with a packing density,  $\eta$ , of  $\pi/\sqrt{12}$  [36]. From this it is possible to show:

$$N_p = \frac{2}{D^2\sqrt{3}} \quad (5)$$

where  $N_p$  is the theoretical number of particles per  $\text{mm}^2$  and  $D$  is the particle diameter (mm) for a HCP arrangement. Using the measured  $D_{50}$  values for each fraction the plot in Fig. 6(c) shows the particle count results normalised a percentage of the theoretical maximum. This brings results for the two factions much closer together with the adhered particle density between 38.5 % and 52.3 % for all specimens. Therefore, by increasing the particle diameter of the powder it is possible to dramatically reduce the number of surface adhered particles simply due to the packing density as a similar percentage of the particles in contact with the surface will adhere regardless of their size.

Fig. 6(c) also reveals competing trends visible between the powder fractions. Fine powder displays a trend similar to that already seen with adhesion decreasing as scan speed increases, whereas coarse powder adhesion increases with increasing scan speed most notably at speeds  $>1500 \text{ mm/s}$ . This may further support the suggestion of mechanical entrapment at higher scan speeds as discussed in Section 3.2. As coarse powder is less favourable for surface adhesion by other mechanisms (Section 3.5), the increased prevalence of entrapment would result in an

increase in coarse particles visible on the surface under high laser scan speeds.

Powder size distributions shown in Fig. 6(d) match fairly closely the particles measured on the specimen surface for both fine and coarse samples. This rules out any significant technique induced error and supports the earlier conclusion that, given the wider as-received size distribution, fine particles will adhere preferentially over coarse particles.

Despite the difference in overall roughness and particle adhesion however, the underlying roughness of the surface without the influence of surface particles is remarkably similar for both powder size fractions as shown in Fig. 7(a). From a process understanding viewpoint, this confirms that the underlying surface roughness is driven largely by the melt track geometry. Once a powder particle has been absorbed in to the melt pool and is liquid then its original geometry appears to have no further influence on the underlying surface roughness.

As with the as-received powder, the upstream and downstream walls of the specimens show different  $R_a$  values, however in this case the values lie much closer together on average with the mean difference only  $2.5 \mu\text{m}$  as shown in Fig. 7(b). The original trend has also been reversed with inlet facing walls showing the greater roughness. This is likely a result of using the RBV system as two recoater guide rails, shown in Fig. 7(c), sit several mm proud of the process plane and disrupt the argon crossflow. Results presented throughout this study suggest that understanding the influence of crossflow on surface roughness, including how it varies when using an RBV style insert, warrants future investigation.

### 3.5. Powder adhesion mechanisms

The experimental results presented have highlighted some of the

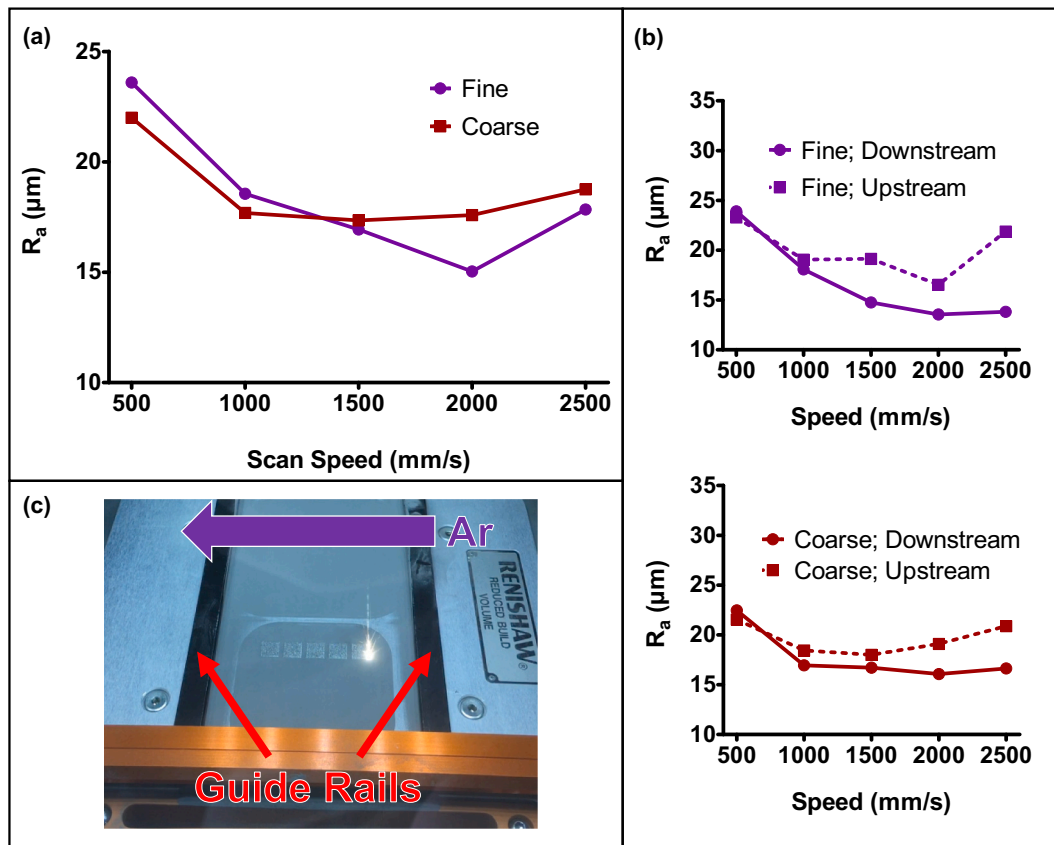


**Fig. 7.** Underlying roughness results for coarse and fine powders processed at 200 W contour laser power; (s) plot showing underlying  $R_a$  against laser scan speed, (b) plots showing comparison of upstream and downstream specimen surface, (c) photograph showing the RBV unit in use within the RenAM500M system; crossflow direction and recoater guide rails have been labelled.

practical relationships between LPBF processing parameters and powder adhered roughness and provides insight into the possible mechanisms responsible. From a general understanding of the process it can be assumed that powder adhesion occurs under one of two conditions: particles in direct contact with the molten pool or particles in contact with the solid material. Each of these regimes presents possible mechanisms for adhesion: at the power/liquid interface, partial melting or wetting may occur, and at the powder/solid interface, solid-state sintering is possible.

Considering partial melting of particles; modelling performed by Haley et al. [37] found that the necessary residence time for metal particles to be in contact with the molten pool before melting decreases with increasing melt superheat temperature, and increases with greater particle diameter. Decreasing melt pool energy input results in a short residence time for adjacent particles and lower melt pool temperature, as such we might expect less particle adhesion by partial melting. This is supported by the results presented in Section 3.2 which shows decreasing surface particle adhesion with increasing laser scan speed. Likewise, the surface particle size distribution suggests a preferential surface adhesion of fine particles that may be due to the shorter necessary residence time for melting of smaller particles compared to larger ones.

Wettability is known to depend on a wide range of factors. However, assuming a similar condition across the powder particles in contact with the molten pool, wettability will increase with melt pool temperature, and hence energy input, as surface tension decreases. This is once again supported by the results presented. Research relating the wetting of metal powder particles with liquid metal is limited, but a general trend shown by Kirchberg et al. [38] suggests that wettability also increases with particle diameter. Given the contrasting trends between how

particle size relates to partial melting and wetting, it could be hypothesised that, under the same processing conditions, particle adhesion at the liquid/powder interface is driven by partial melting for smaller particle size and wetting for larger particle sizes. This remains an interesting avenue for future investigation.

Sintering theory is a complex subject in itself, however traditional texts on the subject conclude that initial sintering rate increases with temperature and decreases with particle size [39]. Once again this behaviour is supported by an observed increase in particle adhesion with input energy and showing an apparent preference for finer rather than coarse particles. Additionally, any sintered connection between a large particle and the LPBF processed surface will be narrower in comparison to its size than that of an equivalent smaller particle. As such, it might be expected that the attachment of large particles to the surface is less stable and prone to simply falling off under its own weight or being removed during the initial washing stage of part removal.

In general, each of these mechanisms tends to favour high energy conditions with both partial melting and sintering promoting a preference for finer particle sizes. Given the complex nature of the surface it is likely that particle adhesion is a combination of all of the above mechanisms with the importance of their respective role determined by the local conditions.

### 3.6. Practical processing considerations

Throughout this research paper, the authors have been careful to note that these specific results are only applicable within the bounds of the experiments carried out due to the high degree of sensitivity of surface roughness to outside influences. The trends observed however can be more widely applied and give rise to a number of practical steps



that can be taken to improve the surface finish of LPBF processed Ti-6Al-4V.

Collectively these results suggest that contour scan parameters should be set at the lowest laser power and highest scan speed combination that still yields a stable and coherent melt track in order to produce the best possible as-built surface finish. This type of optimisation could easily be carried out on a test section of any practical component with minimal equipment or expensive analysis. It should further be noted that contour offset from the hatched region may need to be adjusted to ensure that the low energy processing conditions do not produce sub-surface porosity. Likewise, these conditions should yield the smallest difference between the upstream and downstream surfaces due to argon crossflow.

Finer powder will yield a better surface finish by traditional measurement standards, however particle size does not appear to dramatically influence the underlying surface roughness. Furthermore, using a large particle size may reduce the overall number of particles adhered to the surface and, given that the ratio between particle diameter and neck diameter will be larger, any further surface post-processing may need to be less aggressive. Given possible additional benefits in powder handling and safety, the use of a narrower distribution of coarse powder may yield positive results when combined with a suitable post-processing treatment.

#### 4. Conclusions

The research presented has characterised the surface roughness of LPBF processed Ti-6Al-4V with a variety of contour scan speeds and laser powers. From the results and accompanying discussion presented, the following conclusions can be drawn:

- Traditionally measured surface roughness ( $S_a$ ) tends to decrease with increasing scan speed and to a lesser extent decreasing laser power. At low energy conditions ( $\leq \sim 0.1$  J/mm) roughness increases due to instability of the melt pool.
- Novel image analysis techniques were employed to explore the duality of the LPBF surface. These have shown a similar trend to that of traditionally measured surface roughness in both surface adhered particle and underlying roughness. Use of these techniques has highlighted how traditional line-of-sight measures of roughness may not be adequate on their own in describing this topography.
- Optical size analysis of surface adhered particles showed a finer distribution than the starting powder suggesting preferential attachment of fine particles to the surface.
- Mechanisms driving the surface adhesion of powder have been discussed and related back to the experimental results.
- Gas crossflow was shown to have a large influence on underlying surface roughness with upstream surfaces being  $4.0\ \mu\text{m}$  smoother on average than their downstream counterparts in a traditional processing chamber. The smoothest specimen showed a 19.5 % reduction in underlying  $R_a$  on the upstream surface compared to the downstream.

Finally, a set of practical considerations have been presented with the hope that researchers and AM users will be able to improve the as-built surface finish as well as taking these results as a prompt for further investigation in this area. These include using the lowest possible line-energy for the contour scan whilst still retaining a coherent melt track, and considering how powder particle size distribution may influence post-processing treatments.

#### CRediT authorship contribution statement

**Luke N. Carter:** Conceptualization, Methodology, Software, Formal analysis, Investigation, Writing - Original Draft, Visualization **Victor M. Villapún:** Conceptualization, Investigation, Writing - Review & Editing

**Liam Grover:** Supervision, Funding acquisition, Writing - Review & Editing **Sophie C. Cox:** Conceptualization, Writing - Review & Editing, Supervision, Project administration, Funding acquisition.

All authors have approved of the final article.

#### Declaration of competing interest

The authors declare that they have no known competing financial interests or personal relationships that could have appeared to influence the work reported in this paper.

#### Acknowledgements

The authors would like to acknowledge Daniel Wilmot for technical support during sample production by LPBF and in preparation of the sieved powder.

**Funding:** This work was supported by the EPSRC funded projects: 'Process Design to Prevent Prosthetic Infections' [EP/P02341X/1] and 'Invisible Customisation - A Data Driven Approach to Predictive Additive Manufacture Enabling Functional Implant Personalisation' [EP/V003356/1].

#### References

- [1] Fatemi A, Molaei R, Sharifimehr S, Phan N, Shamsaei N. Multiaxial fatigue behavior of wrought and additive manufactured Ti-6Al-4V including surface finish effect. *Int J Fatigue* 2017;100:347–66.
- [2] Edwards P, Ramulu M. Fatigue performance evaluation of selective laser melted Ti-6Al-4V. *Mater Sci Eng A* 2014;598:327–37.
- [3] Benedetti M, Fontanari V, Bandini M, Zanini F, Carmignato S. Low- and high-cycle fatigue resistance of Ti-6Al-4V ELI additively manufactured via selective laser melting: mean stress and defect sensitivity. *Int J Fatigue* 2018;107:96–109.
- [4] Lowther M, Louth S, Davey A, Hussain A, Ginestra P, Carter L, et al. Clinical, industrial, and research perspectives on powder bed fusion additively manufactured metal implants. *Addit Manuf* 2019;28:565–84.
- [5] Cox SC, Jamshidi P, Eisenstein NM, Webber MA, Burton H, Moakes RJA, et al. Surface finish has a critical influence on biofilm formation and mammalian cell attachment to additively manufactured prosthetics. *ACS Biomater Sci Eng* 2017;3: 1616–26.
- [6] Khorasani M, Gibson I, Ghasemi A, Brandt M, Leary M. On the role of wet abrasive centrifugal barrel finishing on surface enhancement and material removal rate of LPBF stainless steel 316L. *J Manuf Process* 2020;59:523–34.
- [7] Ghorbani J, Li J, Srivastava AK. Application of optimized laser surface re-melting process on selective laser melted 316L stainless steel inclined parts. *J Manuf Process* 2020;56:726–34.
- [8] Scherillo F, Manco E, Hassanin AE, Franchitti S, Pirozzi C, Borrelli R. Chemical surface finishing of electron beam melted Ti6Al4V using HF-HNO<sub>3</sub> solutions. *J Manuf Process* 2020;60:400–9.
- [9] Dixit N, Sharma V, Kumar P. Research trends in abrasive flow machining: a systematic review. *J Manuf Process* 2021;64:1434–61.
- [10] Zhang J, Chaudhari A, Wang H. Surface quality and material removal in magnetic abrasive finishing of selective laser melted 316L stainless steel. *J Manuf Process* 2019;45:710–9.
- [11] Maleki E, Bagherifard S, Bandini M, Guagliano M. Surface post-treatments for metal additive manufacturing: progress, challenges, and opportunities. *Addit Manuf* 2021;37:101619.
- [12] Cozzolino E, Lopresto V, Borrelli D, Caraviello A, Astarita A. An integrated approach to investigate the energy consumption for manufacturing and surface finishing 3D printed Inconel 718 parts. *J Manuf Process* 2022;79:193–205.
- [13] Qiu C, Fones A, Hamilton HGC, Adkins NJE, Attallah MM. A new approach to develop palladium-modified Ti-based alloys for biomedical applications. *Mater Des* 2016;109:98–111.
- [14] Hong M-H, Min B, Kwon T-Y. The influence of process parameters on the surface roughness of a 3D-printed Co-Cr dental alloy produced via selective laser melting. *Appl Sci* 2016;6:401.
- [15] Zhang L, Zhu H, Liu J, Zeng X. Track evolution and surface characteristics of selective laser melting Ti6Al4V. *Rapid Prototyp J* 2018;24:1554–62.
- [16] Yasa E, Deckers J, Kruth J-P. The investigation of the influence of laser re-melting on density, surface quality and microstructure of selective laser melting parts. *Rapid Prototyp J* 2011;17:312–27.
- [17] Frazier WE. Metal additive manufacturing: a review. *J Mater Eng Perform* 2014;23: 1917–28.
- [18] Mumtaz K, Hopkinson N. Top surface and side roughness of Inconel 625 parts processed using selective laser melting. *Rapid Prototyp J* 2009;15:96–103.
- [19] Krol M, Taski T. Surface quality research for selective laser melting of Ti-6Al-4V alloy. *Arch Metall Mater* 2016;61:945–50.
- [20] Strano G, Hao L, Everson RM, Evans KE. Surface roughness analysis, modelling and prediction in selective laser melting. *J Mater Process Technol* 2013;213:589–97.

- [21] Leary M. Surface roughness optimisation for selective laser melting (SLM): accommodating relevant and irrelevant surfaces. Elsevier Inc.; 2016. p. 99–118.
  - [22] Villapún VM, Carter LN, Gao N, Addison O, Webber MA, Shepherd DET, et al. A design approach to facilitate selective attachment of bacteria and mammalian cells to additively manufactured implants. *Addit Manuf* 2020;36:101528.
  - [23] Vandenbroucke B, Kruth J-P. Selective laser melting of biocompatible metals for rapid manufacturing of medical parts. *Rapid Prototyp J* 2007;13:196–203.
  - [24] Spierings AB, Herres N, Levy G. Influence of the particle size distribution on surface quality and mechanical properties in AM steel parts. *Rapid Prototyp J* 2011;17: 195–202.
  - [25] Abele E, Kniepkamp M. Analysis and optimisation of vertical surface roughness in micro selective laser melting. *Surf Topogr-Metrol Prop* 2015;3.
  - [26] Diaz A, Winkelmann L, Michaud J, Terrazas C. Surface finishing and characterization of titanium additive manufacturing components: From rich to smooth surface. The European Powder Metallurgy Association: Shrewsbury; 2016. p. 1–6.
  - [27] Triantaphyllou A, Giusca CL, Macaulay GD, Roerig F, Hoebel M, Leach RK, et al. Surface texture measurement for additive manufacturing. *Surf. Topogr.-Metrol. Prop* 2015;3:024002.
  - [28] Tao P, Li H-x, Huang B-y, Hu Q-d, Gong S-l, Xu Q-y. Tensile behavior of Ti-6Al-4V alloy fabricated by selective laser melting: effects of microstructures and as-built surface quality. *China Foundry* 2018;15:243–52.
  - [29] Grimm T, Wiora G, Witt G. Characterization of typical surface effects in additive manufacturing with confocal microscopy. *Surf Topogr-Metrol Prop* 2015;3: 014001.
  - [30] Singla AK, Banerjee M, Sharma A, Singh J, Bansal A, Gupta MK, et al. Selective laser melting of Ti6Al4V alloy: process parameters, defects and post-treatments. *J Manuf Process* 2021;64:161–87.
  - [31] Rasband WS. ImageJ. In: National Institutes of Health, Bethesda, Maryland, USA; 1997-2018.
  - [32] MATLAB. R2019a (9.6.0.1099231). In: MathWorks, U.S.; 2019.
  - [33] Pockett C. A closer look at the RenAM 500Q (News Release). <https://www.renishaw.com/en/a-closer-look-at-the-renam-500q-44937>; 2019. Renishaw, UK.
  - [34] Ferrar B, Mullen L, Jones E, Stamp R, Sutcliffe CJ. Gas flow effects on selective laser melting (SLM) manufacturing performance. *J Mater Process Technol* 2012; 212:355–64.
  - [35] Schleizer AD, Bonnecaze RT. Displacement of a two-dimensional immiscible droplet adhering to a wall in shear and pressure-driven flows. *J Fluid Mech* 1999; 383:29–54.
  - [36] Hales T. Close packing. In: Hales T, editor. Dense sphere packings: a blueprint for formal proofs. Cambridge: Cambridge University Press; 2012. p. 3–22.
  - [37] Haley JC, Schoenung JM, Lavernia EJ. Modelling particle impact on the melt pool and wettability effects in laser directed energy deposition additive manufacturing. *Mater Sci Eng A* 2019;761:138052.
  - [38] Kirchberg S, Abidin Y, Ziegmann G. Influence of particle shape and size on the wetting behavior of soft magnetic micropowders. *Powder Technol* 2011;207: 311–7.
  - [39] Kang S-J. Sintering. 2005.
- Dr **Luke N. Carter** is a Research Fellow in the Healthcare Technologies Institute and part of the School of Chemical Engineering at the University of Birmingham. He is a metallurgist and engineer, specialising in metal additive manufacturing across a wide range of technologies and alloy systems. Originally carrying out research in the aerospace sector, he now works to use process understanding and the inherent design freedoms of additive manufacturing to further the functionality and patient benefits of medical implants and devices.
- Dr **Victor M. Villapún** is a Research Fellow in the School of Chemical Engineering and the Healthcare Technologies Institute at the University of Birmingham. He aims to exploit the potential of 3D printing in medicine to provide unprecedented customised therapies. This objective is pursued through a keen interest in unearthing the fundamental relationship between manufacturing and biological outcomes with special focus on tackling antibiotic resistance.
- Professor **Liam Grover** is a Professor in Biomaterials Science and Director of the Healthcare Technologies Institute. He completed his PhD at the University of Birmingham before moving to McGill University (Montreal) as a CIHR skeletal health scholar. Returning to Birmingham in 2006, he raised over £30 m to fund research on development and translation of novel medical technologies and is the Founder-Director of the Healthcare Technologies Institute, working to move novel technologies through the translational pipeline. He has published widely on material development to replace tissue function and has filed more than ten patents from osteogenic cements to scar reducing dressings.
- Dr **Sophie C. Cox** is a Senior Lecturer in the School of Chemical Engineering and the Healthcare Technologies Institute (HTI) at the University of Birmingham. Her vision is to improve patient quality of life by innovating new medical devices with unprecedented functionality. These translational activities are underpinned by basic science focused on understanding the biological response to biomaterials and unearthing mechanisms of action.